RESEARCH ARTICLE

Check for updates

In situ surface/interface generation on Cu_2O nanostructures toward enhanced electrocatalytic CO_2 reduction to ethylene using *operando* spectroscopy†

Fangfang Chang, Yongpeng Liu, Juncai Wei, Lin Yang [ID] and Zhengyu Bai [ID] *

Electrocatalytic CO_2 reduction reactions (CO_2RRs), an efficient method of converting carbon dioxide into valuable fuels and chemicals, are attractive as well as challenging. In this work, Cu_2O nanostructures with active facets (face-raised cubic structures (F-Cu_2O) with the (100) facet, octahedral structures (O-Cu_2O) with the (111) facet and edge- and corner-truncated octahedral structures (T-Cu_2O) with both the (100) and (111) facets) were synthesized by a wet chemical reduction method. The surface of Cu_2O nanostructures was reconstructed *in situ* to form Cu_2O/Cu with a highly active interface during the conversion of CO_2 into C_2H_4, which is named F-Cu_2O/Cu, O-Cu_2O/Cu and T-Cu_2O/Cu. The C_2H_4 selectivity on Cu_2O/Cu catalysts follows the order of O-Cu_2O/Cu < F-Cu_2O/Cu < T-Cu_2O/Cu, and the faradaic efficiencies of C_2H_4 are 11.2%, 24.9%, and 58.0% at −1.1 V *versus* the reversible hydrogen electrode, respectively. The experimental results combined with *operando* surface-enhanced Raman spectroscopy reveal that the Cu_2O/Cu interface enhances *CO adsorption and decreases the activation energy of C−C coupling, which is also supported by density functional theory (DFT) calculations. This study will pave a feasible pathway for electrochemical energy storage and convention by crystal facet engineering and interface engineering.

Introduction

Carbon dioxide (CO_2) is greatly responsible for global warming, rising sea levels and other extreme weather patterns, making it imperative to reduce the amount of CO_2 released into the environment by human activities.[1–3] Electrocatalytic CO_2 reduction reactions (CO_2RRs) have received widespread attention due to their functions including but not limited to efficient conversion of CO_2 into value-added chemical feedstocks with high efficiency, providing an opportunity for clean renewable energy storage.[4–6] However, the activity and selectivity of multi-carbon (C_{2+}) products with high commercial values and high energy densities will be severely limited due to the slow kinetics of the C−C coupling step during CO_2RRs.[7,8] The design of catalysts with high activity and selectivity for C_{2+} products is the key to promote the development of this field.

Collaborative Innovation Center of Henan Province for Green Manufacturing of Fine Chemicals, Key Laboratory of Green Chemical Media and Reactions, Ministry of Education, School of Chemistry and Chemical Engineering, Henan Normal University, Xinxiang, Henan 453007, China. E-mail: baizhengyu2000@163.com
†Electronic supplementary information (ESI) available. See DOI: https://doi.org/10.1039/d2qi01977a

Among the various electrocatalysts, copper is a distinct metal catalyst, which can produce considerable amounts of hydrocarbons and alcohols,[9–13] because it can adjust the adsorption energy of intermediates and then promote the C−C coupling to form C_{2+} products.[14–16] C_2H_4 is the main C_{2+} product and an important organic raw material, which is widely used in various industries.[17] Thus far, how to improve the selectivity of Cu-based catalysts for the conversion of CO_2 into C_2H_4 and inhibit the generation of H_2 and C_1 species is the focus of research in terms of experimental and theoretical aspects.[18–22] Extensive research has focused on optimizing compositions,[23–25] morphologies,[26,27] crystal facets[28,29] and other aspects[30–32] of Cu-based catalysts to improve the Faraday efficiency of C_2H_4. For example, Cu nanocubes with three different sizes were synthesized by a colloidal chemistry method to investigate the influence of Cu nanocrystal size on the selectivity and activity of electrocatalytic CO_2 reduction products.[33] The 44 nm Cu nanocubes were optimal for ethylene production with a maximum FE of 41%. Moreover, Cu_2O NPs are more favorable to the selective formation of ethylene with high selectivity as compared to Cu NPs. The controllable construction of Cu^0 and Cu^+ sites was achieved by controlling the loading of cupric oxide on copper phyllosilicate lamella to steer CO_2 electroreduction toward C_2H_4 production with high

performance,[34] which proves that Cu^+ sites are more beneficial to produce ethylene.

For the metal oxide catalyst, the exposed facet surface not only determines the geometry of catalysts but also has a great effect on the electrocatalytic property of catalysts.[35] Cu_2O NPs with different crystal facets show different stabilities and catalytic activities.[36,37] The product of C_2H_4 on Cu_2O NPs depends on diverse crystal facets, which determine the active sites that stabilize crucial intermediates during CO_2RRs. Therefore, crystal facets should be particularly considered in designing efficient CO_2RR catalysts. The studies revealed that Cu^0/Cu^+ sites play a key role in improving C_{2+} products on Cu_2O catalysts.[38] However, there are still no systematic studies on the effect of the Cu_2O/Cu interface with highly active facets in situ generated for electrocatalytic CO_2 reduction to C_2H_4 on Cu_2O nanostructures.

In this work, we prepared Cu_2O catalysts with active facets (F-Cu_2O, O-Cu_2O, T-Cu_2O) using diverse surfactant templates. High-resolution transmission electron microscopy (HR-TEM) exhibits that Cu_2O is enclosed with different facets, which are F-Cu_2O structures with the (100) facet, O-Cu_2O structures with the (111) facet and T-Cu_2O structures with the (111) and (100) facets, respectively. The surface of Cu_2O was reconstructed in situ to form a Cu_2O/Cu interface (F-Cu_2O/Cu, O-Cu_2O/Cu and T-Cu_2O/Cu) during the CO_2RR. The experimental results indicated that the C_2H_4 activity and selectivity are intensely influenced by the surface reconstruction and exposed active facets of Cu_2O catalysts. The C_2H_4 selectivity on Cu_2O/Cu catalysts follows the order of O-Cu_2O/Cu < F-Cu_2O/Cu < T-Cu_2O/Cu, and the faradaic efficiencies of C_2H_4 are 11.2%, 24.9%, and 58.0% at −1.1 V vs. RHE, respectively, relating to the exposure of different highly active facets and in situ generated Cu^+/Cu interface. The experimental results combined with the operando surface-enhanced Raman spectroscopy and DFT calculations confirmed that the presence of Cu^+/Cu interfaces and highly active facets enhances *CO adsorption and decreases the adsorption energy of C–C coupling, thus improving the C_2H_4 selectivity.

Experimental section

Materials

Sodium citrate tribasic dihydrate ($C_6H_5Na_3O_7·2H_2O$), ascorbic acid (AA), sodium hydroxide (NaOH), cupric sulfate pentahydrate ($CuSO_4·5H_2O$), copper chloride dihydrate ($CuCl_2·2H_2O$), lauryl sodium sulfate (SDS) and polyvinyl pyrrolidone (PVP, M_w = 58 000) were all purchased from Aladdin. Glucoses were obtained from Tianli Chemical Reagents. Nafion (5 wt%) were obtained from Aldrich. All gases such as carbon dioxide and nitrogen were obtained from Airgas.

Catalyst preparation

Synthesis of F-Cu_2O. A F-Cu_2O catalyst was prepared by a wet chemical reduction method on the basis of previous reports.[39] Specifically, $C_6H_5Na_3O_7·2H_2O$ (0.1940 g) was first dissolved in 400 mL deionized water and stirred for 20 min. Then, 1 mL $CuSO_4·5H_2O$ (0.77 M) aqueous solution was dropped into this solution. After stirring for 5 minutes, 1 mL NaOH (4.8 M) aqueous solution was slowly added to this mixed solution at room temperature, and 1 mL ascorbic acid (1.2 M) was added under stirring for 30 min to form a yellow solution. The solution was centrifuged after standing aged for 6 hours, washed three times with ethanol and deionized water and finally dried in a vacuum dryer.

Synthesis of O-Cu_2O. In a typical process,[40] 9.67 g PVP was added to a round-bottom flask (250 mL) containing 100 mL $CuCl_2·2H_2O$ (1 mM) aqueous solution and stirred continuously in a 60 °C water bath. Then, 10 mL NaOH (2 M) aqueous solution was subsequently added to the round-bottom flask and stirred continuously for 30 min. Glucose (1.2 g) was added to this mixture and stirred vigorously for 3 h. All of the processes were maintained at 60 °C. The precipitates were centrifuged three times in deionized water and anhydrous ethanol, and dried under vacuum at 60 °C for 6 h.

Synthesis of T-Cu_2O. In a typical synthesis,[40] 0.085 g $CuCl_2·2H_2O$ (5.65 mM) was added to 88.2 mL solution containing 0.87 g SDS (34.01 mM) and then stirred vigorously at 60 °C for 10 min. After that, 1.8 mL NaOH (1 M) and 5 mL glucose (0.1 M) were rapidly added to this solution and maintained under magnetic stirring for 1 h. The color of the suspension gradually changed to orange. The orange product was collected via centrifugation, washed several times with ethanol and deionized water to remove excess SDS, and finally dried under vacuum for further use.

Characterization of the catalysts

TEM was performed using a JEM 2100 to characterize the morphologies and size of the as-synthesized Cu_2O catalysts. An X′ Pert3 Powder instrument at 45 kV and 40 mA was used to analyze the powder X-ray diffraction (XRD) pattern of Cu_2O catalysts. X-ray photoelectron spectroscopy (XPS) and Cu LMM spectra were recorded using a Thermo Scientific K-Alpha instrument to obtain the structure of catalysts. The chemical structures of Cu_2O samples were analyzed by Infrared Spectroscopy (IR).[41,42]

Electrocatalytic activity measurements

The catalyst ink was prepared by dispersing 20 mg Cu_2O and 5 μL of Nafion solution (5 wt%) in 1 mL isopropanol for at least 30 min by ultrasonication.[43] Subsequently, the ink was coated onto the polished glassy carbon electrode (diameter: 3 mm; area: 0.07 cm²) surface. The electrode was then dried in ambient air to obtain the working electrode for later electrochemical performance tests. Electrochemical performance tests were operated on a workstation (CHI 760E) equipped with an air-tight three-electrode cell, which used a glassy carbon (GC) electrode coated with catalysts as the working electrode. A Pt sheet and a Ag/AgCl (saturated KCl) electrode were used as the counter and reference electrodes, respectively. First, 0.1 M $KHCO_3$ solution was used as the electrolyte for all electrochemical CO_2RRs. The solution in the cathodic cell was satu-

This journal is © the Partner Organisations 2023

Inorg. Chem. Front., 2023, **10**, 240–249 | **241**

rated with N_2 or CO_2 before electrochemical testing and 20 sccm flow rate was maintained during the CO_2RR. The potential was converted into the reversible hydrogen electrode (RHE) as follows:

$$E(vs. \text{ RHE}) = E(vs. \text{ Ag AgCl}) + 0.197 \text{ V} + 0.0591 \text{ V} \times \text{pH}$$

The gaseous products (*i.e.*, H_2, CO, CH_4 and C_2H_4) were quantified using a gas chromatograph (GC, Panna) equipped with a thermal conductivity detector (TCD) and a flame ionization detector (FID). The GC was directly linked to an electrochemical cell for online analysis. The faradaic efficiency of gaseous products was calculated using the following equation:[44]

$$\text{FE} = \frac{n \times F \times C_i \times G \times p}{R \times T \times j}$$

where n is the number of electrons required to produce a molecular product (*e.g.*, 2, 2, 8, and 12 e^- for CO, H_2, CH_4 and C_2H_4), F is the Faraday constant (96 485 C mol^{-1}), C_i is the measured concentration of the products by GC, G is the gas flow rate, j is the current density, p is the atmospheric pressure, 1.013×10^5 Pa, $R = 8.314$ J mol^{-1} K^{-1}, and $T = 273.15$ K.

The liquid mixture was analyzed by 1H nuclear magnetic resonance, which was recorded using a Bruker Avance NEO 400 MHz spectrometer in deuterium oxide-d$_2$ with DMSO as internal standards.[9]

Double-layer capacitance (C_{dl})

The C_{dl} value was relative to the electrochemical active surface area. The C_{dl} value was estimated by cyclic voltammetry (CV) to measure the relationship between the scanning rate and capacitive current density. The potential of CV ranged from 0.4 V to 0.5 V *vs.* RHE. The C_{dl} value was estimated by plotting Δj ($j_a - j_c$) at −0.15 V *vs.* RHE against the scan rates (j_a = anodic current density and j_c = cathodic current density). The slope of C_{dl} was estimated to be twice that of C_{dl}.[41]

In situ surface-enhanced Raman spectroscopy (SERS)

The potential-dependent SERS was conducted by combining an *in situ* surface enhanced Raman spectrometer[25] with an optical microscope (excitation wavelength 633 nm, sample power 3 mW). A glass carbon electrode, a Pt wire and a Ag/AgCl (saturated KCl) electrode were used as the working, counter and reference electrodes, respectively. During the SERS test, 0.1 M $KHCO_3$ saturated by high-purity CO_2 was continuously fed into the electrolytic cell. Raman spectra were recorded in the range of 100 to 3000 cm^{-1} using a 633 nm laser. The Raman spectra were acquired at about 10 min after the potential was initially applied.

DFT calculations

CASTEP calculation of Materials Studio was used for DFT calculations. We used the Perdew–Burke–Ernzerhof (PBE) exchange correlation functional of the generalized gradient approximation (GGA) with a cutoff energy of 450 eV. A custo-

mized $(3 \times 3 \times 1)$ k-point grid was adopted for all the calculations.[45] The convergence criterion of residual force and energy was set to 0.03 eV Å^{-1} and 10^{-5} eV in order to avoid the interaction between periodic units during structural relaxation, and the vacuum space in the z direction is larger than 20 Å. The Cu_2O/Cu interface model is supported by a two-layer Cu (100)-(3×3), four-layer Cu_2O(100)-(2×2) slab or nine-layer Cu_2O(111)-(2×2) slab with 15 Å vacuum space. The change in free energy was calculated by the computational hydrogen electrode (CHE) method.[46]

Results and discussion

Composition and morphology of Cu_2O nanocatalysts

Cu_2O nanostructures with highly active facets were successfully prepared by a wet chemical reduction method with diverse surfactants. In this process, surfactants play a key role in regulating the exposed crystal facets of Cu_2O by changing the crystallization agent, especially meaning that different types and amounts of surfactant applications lead to crystal growth differential rate and direction, thus laying the foundation for the ultimate morphology of Cu_2O nanostructures. The morphology of as-synthesized Cu_2O was investigated by TEM. As shown in representative TEM images, the as-synthesized F-Cu_2O, O-Cu_2O, and T-Cu_2O nanostructures exhibit the desired face-raised cubic structure (Fig. S1a, ESI†), octahedral structure (Fig. S2a, ESI†) and edge- and corner-truncated octahedral structure (Fig. S3, ESI†). In detail, Fig. S1b† shows the HR-TEM image of the F-Cu_2O catalyst enclosed with excellent crystallinity of the (100) facets. Besides, the F-Cu_2O catalyst possesses uniform particle size distribution, as shown in Fig. S1c.† Similarly, the O-Cu_2O catalyst is composed of the (111) facet (Fig. S2b, ESI†) and the T-Cu_2O catalyst is composed of the (100) and (111) facets (Fig. 1a and d), which are related to the types and amounts of surfactants (PVP and SDS) during the synthesis process. The different d-spacing values of lattice fringes from HR-TEM images also confirm the existence of the abovementioned crystal facets. Fig. 1a, d, and S3† give the TEM, high HR-TEM, and EDS-elemental mapping images of T-Cu_2O viewed along the different zone axis directions, from which it could be found that the T-Cu_2O catalyst is composed of 18 (100) facets and 8 (111) facets. Fig. S3b and e† show the HR-TEM images of the T-Cu_2O catalyst and show the distinct lattice fringes with d spacings of 2.13 and 2.45 Å, which correspond to the (100) and (111) lattice facets of T-Cu_2O. The lattice plane directions are also in compliance with the respective particle orientation. For the F-Cu_2O catalyst, it shows a cubic shape, which can be assumed that the shape of F-Cu_2O is enclosed with 6 protruded (100) facets with 12 edges. The lattice fringe of the F-Cu_2O catalyst is 2.13 Å and matches the (100) facet, as shown in Fig. S1b.† For the O-Cu_2O catalyst, it is enclosed with 8 (111) facets, with a lattice spacing of 2.45 Å corresponding to the (111) facet. Cu_2O nanostructures with different morphologies and facets were characterized by EDS-elemental mapping technique. Fig. S1c, 2c and 3† indicate
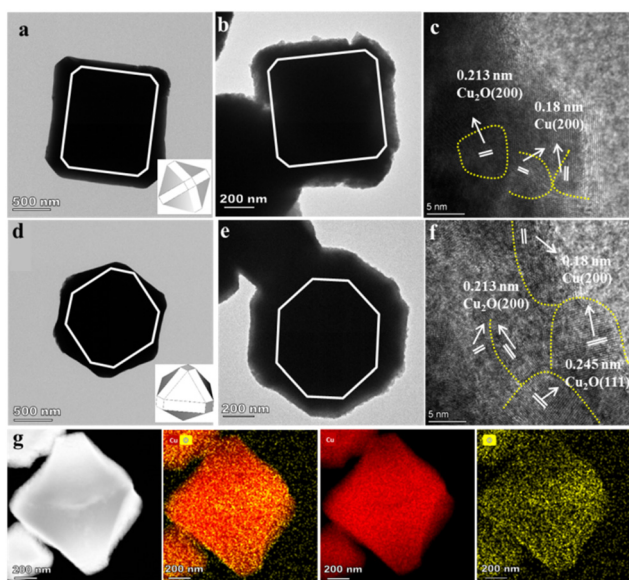
242 | *Inorg. Chem. Front.*, 2023, **10**, 240–249

This journal is © the Partner Organisations 2023

Fig. 1 Structural characterization of catalysts. The TEM images of T-Cu_2O viewed along the (a) [100] and (d) [111] directions, and the (b and e) TEM images, (c and f) HR-TEM images, (g) HAADF-STEM and elemental mapping images (Cu species were in red, and O species were in yellow) of surface-reconstructed T-Cu_2O samples after reduction at −1.1 V vs. RHE.

that Cu and O elements are averagely distributed through Cu_2O catalysts.

The catalysts are reduced at −1.1 V vs. RHE to investigate the surface reconstruction of Cu_2O and the formation of Cu^+/Cu^0 interface during CO_2RRs. TEM, HR-TEM and EDS-elemental mapping images of F-Cu_2O, O-Cu_2O and T-Cu_2O catalysts after stability test during CO_2RRs are shown in Fig. 1, S1d–f and S2d–f.† It is clear that Cu_2O structures are well preserved and the Cu^+/Cu^0 interface was formed, as revealed from the lattice fringes (Fig. S1e, S2e, 1c and f†). The surface reconstruction of F-Cu_2O, O-Cu_2O and T-Cu_2O catalysts is named F-Cu_2O/Cu, O-Cu_2O/Cu and T-Cu_2O/Cu.

XRD and XPS techniques were used to investigate the crystalline state and chemical valence states of Cu_2O before and after surface reconstruction. As shown in Fig. 2a–c, the three

samples with different exposed active facets are in good agreement with the simulated diffraction patterns of Cu_2O (PDF#05-0667) in the range of 29.55°–77.32°, and the XRD results also show that all the as-prepared Cu_2O catalysts manifest two intensive peaks at 36.4° and 42.3°, which belong to the (111) and (200) facets of Cu_2O before CO_2RRs. In addition, all these peaks are almost unchanged after CO_2RRs and two new peaks appeared at 43.3° and 50.43°, corresponding to the (111) and (200) facets of metallic Cu (PDF# 04-0836). The XRD results demonstrate that the structure of the as-synthesized Cu_2O catalyst is relatively stable, and partial Cu_2O is reduced to Cu, which is consistent with the TEM images. The chemical state of F-Cu_2O, O-Cu_2O, and T-Cu_2O catalysts was further studied by XPS measurement. The XPS results supported by XRD before CO_2RRs show that there are O and Cu elements in all three samples, among which Cu^+ species appeared in the Cu 2p spectrum, as shown in Fig. S4.† Fig. S4a† reveals that Cu_2O catalysts have a similar sharp Cu^+ peak at 932.5 eV. The presence of satellite peaks at 945.8 eV also proves the presence of Cu^+.[47] In addition, low-intensity characteristic peaks at 933.5 eV and 953.0 eV are associated with Cu^{2+} $2p_{3/2}$ and Cu^{2+} $2p_{1/2}$, respectively, which indicates that there is a small amount of CuO in the Cu_2O nanostructure, due to the natural surface oxidation during the ex situ XPS measurement.[48] Subsequently, the valence states of samples immediately after CO_2RRs was characterized by XPS. After CO_2RRs, the weak peak of Cu^{2+} disappeared (Fig. 2d) and had a main Cu $2p_{3/2}$ feature at 932.5 eV, which can be vested in either Cu_2O (Cu^+) or Cu (Cu^0) but is not distinguishable, as the binding energies between Cu^+ and Cu^0 differ by only 0.1 eV (Fig. 2d).[49] The characteristic peak at 531 eV is related to the existence of lattice oxygen and oxygen vacancies (Fig. 2e). In addition, the Raman spectra (Fig. S5†) of the reconstructed Cu_2O catalysts exhibit an absorption peak around 150 cm^{-1}, which could be ascribed to an oxygen defect excited mode. Fig. 2f provides the Cu LMM spectra to further distinguish Cu^+ and Cu^0. The characteristic peak of Cu^0 at 568.0 eV is presented in the Cu LMM spectrum (Fig. 2f) and the main peak of Cu^+ is retained (569.9 eV), which further indicates that Cu_2O is reduced only on the surface, but the bulk structure is relatively stable. The surface compositions of Cu^+ and Cu^0 on the different Cu_2O catalysts after CO_2RRs are clearly distinguished by Cu LMM spectra and XPS analysis, as shown in Table S1.† The Cu^+ content of T-Cu_2O catalyst is significantly higher than that of F-Cu_2O and O-Cu_2O catalysts after surface reconstruction.

Catalyst performance

The electrocatalytic CO_2RR performances of F-Cu_2O/Cu, O-Cu_2O/Cu and T-Cu_2O/Cu were also investigated in CO_2-saturated 0.1 M $KHCO_3$ (pH = 6.8) aqueous solutions in a typical air-tight three-electrode electrochemical system. The electrocatalytic activity of Cu_2O/Cu for CO_2RRs is assessed in a N_2 and CO_2-saturated 0.1 M $KHCO_3$ solution by linear sweep voltammetry (LSV), respectively, and the LSV curves are recorded with a sweep speed of 20 mV s^{-1} in the potential range from 0 to −1.4 V (vs. RHE). Obviously, the total current densities of
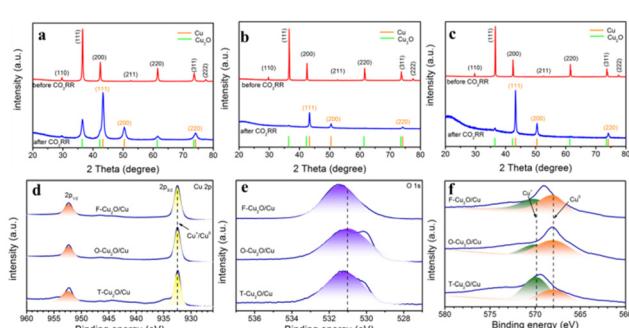

Fig. 2 XRD patterns of catalysts: (a) F-Cu_2O, (b) O-Cu_2O and (c) T-Cu_2O. XPS spectra of (d) Cu 2p, (e) O 1s and (f) Cu LMM of F-Cu_2O, O-Cu_2O and T-Cu_2O after CO_2RRs at −1.1 V vs. RHE until stable.

This journal is © the Partner Organisations 2023

Inorg. Chem. Front., 2023, **10**, 240–249 | **243**

three Cu_2O/Cu catalysts are all higher in CO_2-saturated electrolytes than those in N_2-saturated electrolytes, as shown in Fig. S6,† which suggests that the electrocatalytic activity of the catalysts for CO_2RRs is better than that for hydrogen evolution reactions (HERs).[50] In addition, the LSV curves (Fig. 3a) exhibit the onset potentials decreasing following the order of T-Cu_2O/Cu > F-Cu_2O/Cu > O-Cu_2O/Cu, indicating that the onset potential and the electrocatalytic activity of T-Cu_2O/Cu catalyst are higher than those of the other two catalysts. Moreover, the electrochemical double-layer capacitance measurement was implemented to evaluate the electrochemical surface area (ECSA) of Cu_2O/Cu catalysts. According to CV curves at different scanning rates, the ECSA of catalysts was obtained through calculating the double-layer capacitance (C_{dl}) of the catalysts. T-Cu_2O/Cu exhibits the largest ECSA value among the three catalysts (Fig. S7†), which indicates that T-Cu_2O/Cu can provide a more accessible active site as compared with the other catalysts. Gas chromatography (GC) and ^1H NMR spectroscopy (Fig. S8, S9 and Table S2†) are used to analyze the effluent gaseous products and liquid products formed in CO_2RRs at different applied potentials between −0.8 and −1.2 V vs. RHE. The products from CO_2RR and the relevant faradaic efficiencies are displayed in Fig. 3b. Compared with the electrocatalytic performances of Cu_2O/Cu catalysts, T-Cu_2O/Cu exhibits better activity and electrocatalytic conversion efficiency than those of F-Cu_2O/Cu and O-Cu_2O/Cu. Specifically, the total faradaic efficiency reaches 97.8% over T-Cu_2O/Cu at −1.1 V vs. RHE. Notably, the C_{2+} products of CO_2RRs are mainly C_2H_4 and C_2H_5OH on the three Cu_2O/Cu samples and the maximum FE of C_{2+} products achieve 69.0% at T-Cu_2O/Cu. The FE values of C_2H_4 and H_2 on T-Cu_2O/Cu as a function of applied potential are compared in Fig. 3c. As presented, T-Cu_2O/Cu displays the highest selectivity to C_2H_4, achieving 58.0% at −1.1 V vs. RHE, while F-Cu_2O/Cu and

O-Cu_2O/Cu reach 24.9% and 11.2%, respectively. The evolution of H_2 is inhibited by T-Cu_2O/Cu, and the FE of H_2 is less than 30% in the whole potential range. Therefore, the T-Cu_2O/Cu catalyst has high selectivity for CO_2RRs to C_{2+} products. The detailed faradaic efficiencies for all products at various potentials are listed in Fig. S10.† It is apparently noted that the selectivity of the products varied with the applied potentials. CO was found to be the major product at relatively low overpotentials (from −0.8 to −0.9 V vs. RHE). With the applied potential being more negative, the FEs for CO production decrease and the FEs for ethylene production increase. This is consistent with the widely accepted hypothesis that the adsorbed CO is an intermediate in the formation of C_{2+} products.[51,52] In addition, the electrocatalytic performance of T-Cu_2O/Cu is significantly better than that of Cu-based catalysts reported in the literature under similar experimental conditions (Table S3†).[53–61]

To gain more accurate facet features of the Cu_2O catalysts, we applied electrochemical adsorption of OH^- on the Cu_2O catalysts before and after reconstruction, which take into account their facet-dependent OH^- adsorption behaviors.[62] As shown in Fig. S11a,† the cyclic voltammetry (CV) curves of the three Cu_2O catalysts before reconstruction did not exhibit the OH^- adsorption/desorption peaks. As for the reconstructed Cu_2O samples, the CV curves show OH^- adsorption peaks at −0.34 and −0.43 V vs. RHE for F-Cu_2O/Cu and O-Cu_2O/Cu, which can be assigned to the OH^- adsorption on the Cu(100) and Cu(111) surfaces,[63] respectively. Such two adsorption peaks exist simultaneously on the T-Cu_2O/Cu catalyst, manifesting that T-Cu_2O/Cu is dominated by both the {100} and {111} facets (Fig. S11b†). Above all, it can be considered that metallic Cu with the corresponding crystal facets is generated on the surface of the reconstructed Cu_2O samples.

The stability is an important factor during CO_2RRs in practical application. The electrocatalytic stability of the T-Cu_2O/Cu catalyst for CO_2RR was examined under −1.1 V vs. RHE for 10 h in 0.1 M $KHCO_3$ by chronopotentiometry technique. The stability result of T-Cu_2O/Cu catalyst is given in Fig. 3d, which implies that the T-Cu_2O/Cu catalyst has good working stability. It is also noticeable that the increase in $FE_{C_2H_4}$ is greatest between initial one and two hours and then decreases slightly. Furthermore, the FE for C_2H_4 reaches a maximum value of 58.0% when the reduction time is 2 h, indicating that CO_2RR performance is stable in the long-term test. The electrocatalytic durability of the T-Cu_2O/Cu catalyst was further valued by cycling 2000 cycles between −1.4 and 0 V vs. RHE at a scan rate of 50 mV s^{-1}. As shown in Fig. S12,† the test results showed only a slight decrease in activity at high potentials. The IR and PXRD patterns (Fig. S13 and 14†) of the recycled catalysts showed that the three catalysts can be well maintained during the catalytic reaction.

CO_2 electroreduction mechanisms on Cu_2O/Cu catalysts

It is widely accepted that CO_2RRs to multi-carbon products experience a critical CO dimerization step.[64,65] We thus compared the coverage of surface-adsorbed CO (*CO) on T-Cu_2O/

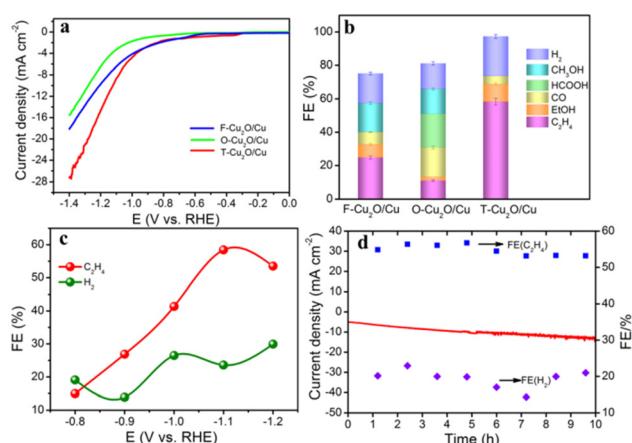**Fig. 3** Electrocatalytic CO_2RR performance. (a) LSV curves in a 0.1 M $KHCO_3$ aqueous solution saturated with CO_2 for Cu_2O/Cu catalysts; (b) faradaic efficiencies of various products at −1.1 V vs. RHE; (c) contrast of $FE_{C_2H_4}$ and FE_{H_2} for CO_2RRs catalyzed by T-Cu_2O/Cu at different applied potentials (−0.8 V to −1.2 V vs. RHE); and (d) stability of T-Cu_2O/Cu at a potential of −1.1 V vs. RHE for 10 h.

244 | Inorg. Chem. Front., 2023, 10, 240–249

This journal is © the Partner Organisations 2023

Cu, F-Cu$_2$O/Cu, and O-Cu$_2$O/Cu catalysts by *in situ* Raman spectroscopy at an open circuit potential (OCP) and between −0.5 and −0.9 V *vs.* RHE from 250 to 650 cm^{-1} and 1550 to 2800 cm^{-1}, and this technique showed good sensitivity to *CO intermediates. In *in situ* Raman spectroscopy (Fig. S15†), low potentials were employed because the intermediate could be retained and there were not many bubbles on the electrode to affect the Raman spectral signal. As shown in Fig. 4a–c, the characteristic peaks were located at 218, 527 and 623 cm^{-1}, corresponding to Cu$_2$O at the OCP. At the reduction potential from −0.5 V to −0.9 V *vs.* RHE, the peaks at 360, 532 and 1070 cm^{-1} were assigned to the Cu–CO stretching mode, Cu–CO, the adsorbed OH group (vibration of Cu–OH), and CO$_3^{2-}$ modes,[66] respectively, indicating the presence of Cu. XRD and XPS results also confirmed the existence of Cu peaks (Fig. 2). With the increase in applied potentials, two noticeable Raman peaks appeared on the T-Cu$_2$O/Cu electrode (Fig. 4d), where the peak at ∼2070 cm^{-1} originated from the stretching vibration mode of absorbed CO* at the top site.[67,68] The peak at ∼1980 cm^{-1} could be attributable to the interaction between absorbed CO* intermediates,[69,70] which benefited C$_{2+}$ production. However, as for F-Cu$_2$O/Cu and O-Cu$_2$O/Cu, the *CO peak at a lower shift was so weak that could not be observed clearly. There was only the single mode at ∼2070 cm^{-1}, manifesting a less favorable C–C coupling on the two electrodes (Fig. 4e and f), which was consistent with the electrochemical CO$_2$RR results that it mainly produced CH$_3$OH/H$_2$ and could not produce much C$_2$H$_4$ products.[71] Moreover, both Raman signals disappeared on the T-Cu$_2$O/Cu electrode at high potentials, indicating that these intermediates reacted to CO$_2$ reduction kinetics at very fast rates.

DFT calculation

To gain deeper insights into the high selectivity of C$_2$H$_4$ on T-Cu$_2$O/Cu with the (111)/(100) facet compared with F-Cu$_2$O/Cu with the (100) facet and O-Cu$_2$O/Cu with the (111) facet catalysts, the DFT calculation was carried out to study the free energy of *CO intermediates on Cu$_2$O/Cu with the (111), (100) and (111)/(100) facet. F-Cu$_2$O/Cu(100), O-Cu$_2$O/Cu(111) and T-Cu$_2$O/Cu(111)/(100) models were built based on our HR-TEM
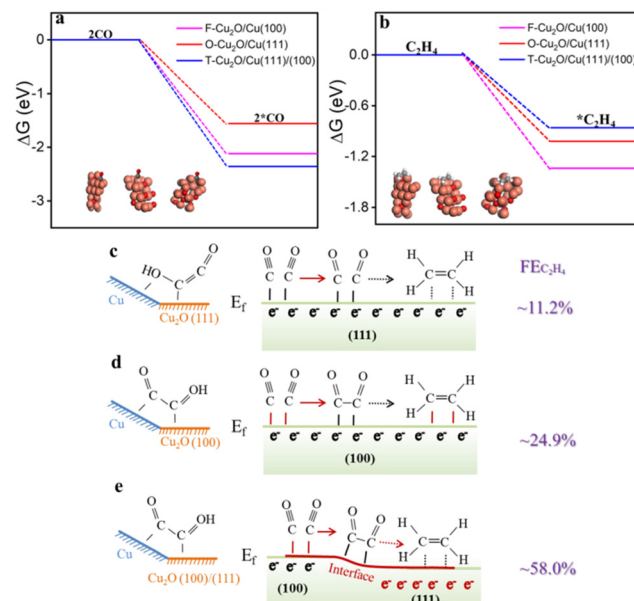

Fig. 4 *In situ* Raman spectra of CO$_2$RR over (a and d) T-Cu$_2$O/Cu, (b and e) F-Cu$_2$O/Cu and (c and f) O-Cu$_2$O/Cu as a function of the applied potentials.

Fig. 5 Adsorption energies of (a) CO and (b) C$_2$H$_4$ on F-Cu$_2$O/Cu(100), O-Cu$_2$O/Cu(111) and T-Cu$_2$O/Cu(111)/(100) catalysts. Formation of C$_2$H$_4$ on (c) O-Cu$_2$O/Cu(111), (d) F-Cu$_2$O/Cu(100) and (e) T-Cu$_2$O/Cu(111)/(100) catalysts.

results to explore the mechanism of CO$_2$RRs in depth. Fig. 5 shows that the adsorption of *CO intermediate on the surface of Cu$_2$O/Cu(100) and Cu$_2$O/Cu(111)/(100) catalysts was stronger than that on Cu$_2$O/Cu(111), which would subsequently promote the C–C coupling to produce C$_{2+}$ products in the CO$_2$RR process, and was consistent with the *in situ* Raman result (Fig. 4d–f). In addition, the adsorption of C$_2$H$_4$ on Cu$_2$O/Cu(111)/(100) and Cu$_2$O/Cu(111) was weaker than that on Cu$_2$O/Cu(100), indicating that Cu$_2$O/Cu(100) could promote the C–C coupling to generate C$_{2+}$ products, but the C$_{2+}$ products formed (*e.g.*, C$_2$H$_4$) were difficult to escape from the surface of Cu$_2$O/Cu(100) due to the strong adsorption ability of C$_2$H$_4$. Associated with the experimental results, the synergistic effect of Cu^0 and Cu$^+$ was the activation of CO$_2$ on the Cu^0 site to promote the following electron transfers, and strengthen the *CO adsorption on the Cu$^+$ site to further facilitate C–C coupling. According to Cu LMM results after reconstruction (see Table S1, ESI†), the T-Cu$_2$O/Cu sample has more Cu$^+$ active sites than the other two catalysts, so *CO adsorption on the T-Cu$_2$O/Cu catalyst is stronger and can further promote C–C coupling.[32] Although the adsorption ability of the *CO intermediate on O-Cu$_2$O/Cu(100) was low, C$_2$H$_4$ could be desorbed from the surface of O-Cu$_2$O/Cu(100), due to its weak adsorption energy. Moreover, the *CO intermediate could not only be strongly adsorbed on the surface of T-Cu$_2$O/Cu(111)/(100) to facilitate the C–C coupling, but also C$_2$H$_4$ formed was easily desorbed from the surface of T-Cu$_2$O/Cu(111)/(100). Besides, T-Cu$_2$O/Cu(111)/(100) had better catalytic performance than F-Cu$_2$O/Cu(100) and O-Cu$_2$O/Cu(111), which might be related to the fact that the Fermi energy level of Cu$_2$O on the (111)
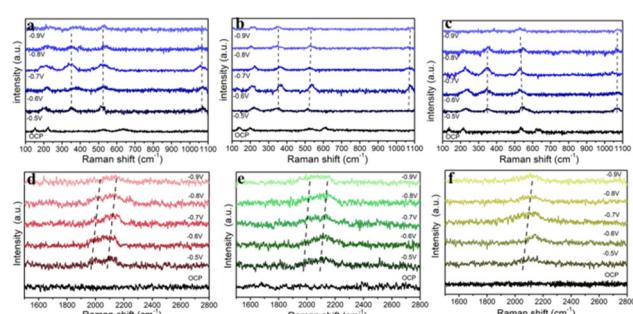
This journal is © the Partner Organisations 2023

Inorg. Chem. Front., 2023, **10**, 240–249 | **245**

facet was lower than that on the (100) facet, which promoted the charge transfer between the Cu_2O (111) and (100) facets and further facilitated the multi-electron participation kinetics of C_2H_4 formation (Fig. 5c–d).

Conclusion

In summary, F-Cu_2O, O-Cu_2O and T-Cu_2O catalysts enclosed with the (111), (100) and (111)/(100) facets have been synthesized by a wet chemical reduction method, which has been reconstructed *in situ* to form F-Cu_2O/Cu(100), O-Cu_2O/Cu(111) and T-Cu_2O/Cu(111)/(100) catalysts. The experimental results indicated that the T-Cu_2O/Cu catalyst shows maximum $FE_{C_2H_4}$ values of 58.0% for CO_2RRs at −1.1 V *vs.* RHE, which is much better than those of the F-Cu_2O/Cu catalyst (24.9%) and O-Cu_2O/Cu catalyst (11.2%). The combination of *in situ* spectroscopy, electrochemical measurement and DFT calculation results revealed that the faradaic efficiencies of C_2H_4 on reconstructed Cu_2O catalysts is related to the exposure of highly active facets and the synergistic effect of Cu^+ and Cu^0 (Cu^+/Cu^0) generated *in situ*, which can enhance the *CO adsorption and decrease the activation energy of C–C coupling, thus improving the selectivity of the C_2H_4. This study will pave a feasible pathway for electrochemical energy storage and convention by crystal facet engineering and interface engineering.

Conflicts of interest

The authors declare no conflict of interest.

Acknowledgements

References

1 M. He, Y. Sun and B. Han, Green carbon science: Scientific basis for integrating carbon resource processing, utilization, and recycling, *Angew. Chem., Int. Ed.*, 2013, **52**, 9620–9633.

2 Q. Lu, J. Rosen, Y. Zhou, G. S. Hutchings, Y. C. Kimmel, J. G. Chen and F. Jiao, A selective and efficient electrocatalyst for carbon dioxide reduction, *Nat. Commun.*, 2014, **5**, 3242.

3 W. Wang, L. Shang, G. Chang, C. Yan, R. Shi, Y. Zhao, G. I. N. Waterhouse, D. Yang and T. Zhang, Intrinsic carbon-defect-driven electrocatalytic reduction of carbon dioxide, *Adv. Mater.*, 2019, **31**, 1808276.

4 K. Ye, A. Cao, J. Shao, G. Wang, R. Si, N. Ta, J. Xiao and G. Wang, Synergy effects on Sn-Cu alloy catalyst for efficient CO_2 electroreduction to formate with high mass activity, *Sci. Bull.*, 2020, **65**, 711–719.

5 F. F. Chang, M. L. Xiao, R. F. Miao, Y. P. Liu, M. Y. Ren, Z. C. Jia, D. D. Han, Y. Yuan, Z. Y. Bai and L. Yang, Copper-based catalysts for electrochemical carbon dioxide reduction to multicarbon products, *Electrochem. Energy Rev.*, 2022, **5**, 4.

6 F. Yang, A. Chen, P. L. Deng, Y. Zhou, Z. Shahid, H. Liu and B. Y. Xia, Highly efficient electro conversion of carbon dioxide into hydrocarbons by cathodized copper-organic frameworks, *Chem. Sci.*, 2019, **10**, 7975–7981.

7 L. Fan, C. Xia, F. Yang, J. Wang, H. Wang and Y. Lu, Strategies in catalysts and electrolyzer design for electrochemical CO_2 reduction toward C_{2+} products, *Sci. Adv.*, 2020, **6**, eaay3111.

8 Y. Zheng, A. Vasileff, X. Zhou, Y. Jiao, M. Jaroniec and S. Z. Qiao, Understanding the roadmap for electrochemical reduction of CO_2 to multi-carbon oxygenates and hydrocarbons on copper-based catalysts, *J. Am. Chem. Soc.*, 2019, **141**, 7646–7659.

9 D. Gao, I. Sinev, F. Scholten, R. M. Aran-Ais, N. J. Divins, K. Kvashnina, J. Timoshenko and B. R. Cuenya, Selective CO_2 electroreduction to ethylene and multicarbon alcohols via electrolyte-driven nanostructuring, *Angew. Chem., Int. Ed.*, 2019, **58**, 17047–17053.

10 D. Kim, C. S. Kley, Y. Li and P. Yang, Copper nanoparticle ensembles for selective electroreduction of CO_2 to C_2−C_3 products, *Proc. Natl. Acad. Sci. U. S. A.*, 2017, **114**, 10560–10565.

11 S. Nitopi, E. Bertheussen, S. B. Scott, X. Liu, A. K. Engstfeld, S. Horch, B. Seger, I. E. L. Stephens, K. Chan, C. Hahn, J. K. Nørskov, T. F. Jaramillo and I. Chorkendorff, Progress and perspectives of electrochemical CO_2 reduction on copper in aqueous electrolyte, *Chem. Rev.*, 2019, **119**, 7610–7672.

12 C. Xu, X. Zhi, A. Vasileff, D. Wang, B. Jin, Y. Jiao, Y. Zheng and S. Z. Qiao, Highly selective two-electron electrocatalytic CO_2 reduction on single-atom Cu catalysts, *Small Struct.*, 2021, **2**, 2000058.

13 D. Zang and H. Wang, Polyoxometalate-based nanostructures for electrocatalytic and photocatalytic CO_2 reduction, *Polyoxometalates*, 2022, **1**, 9140006.

14 K. P. Kuhl, E. R. Cave, D. N. Abra and T. F. Jaramillo, New Insights into the electrochemical reduction of carbon dioxide on metallic copper surfaces, *Energy Environ. Sci.*, 2012, **5**, 7050–7059.

15 H. Mistry, A. S. Varela, C. S. Bonifacio, I. Zegkinoglou, I. Sinev, Y. W. Choi, K. Kisslinger, E. A. Stach, J. C. Yang and P. Strasser, Highly selective plasma-activated copper catalysts for carbon dioxide reduction to ethylene, *Nat. Commun.*, 2016, **7**, 12123.

16 F. S. Roberts, K. P. Kuhl and A. Nilsson, High Selectivity for Ethylene from carbon dioxide reduction over copper nanocube electrocatalysts, *Angew. Chem., Int. Ed.*, 2015, **54**, 5179–5182.

246 | *Inorg. Chem. Front.*, 2023, **10**, 240–249

This journal is © the Partner Organisations 2023

17 S. Sen, D. Liu and G. T. R. Palmore, Electrochemical reduction of CO_2 at copper nanofoams, *ACS Catal.*, 2014, **4**, 3091–3095.

18 O. A. Baturina, Q. Lu, M. A. Padilla, L. Xin, W. Z. Li, A. Serov, K. Artyushkova, P. Atanassov, F. Xu, A. Epshteyn, T. Brintlinger, M. Schuette and G. E. Collins, CO_2 electroreduction to hydrocarbons on carbon-supported Cu nanoparticles, *ACS Catal.*, 2014, **4**, 3682–3695.

19 J. Kim, W. Choi, J. W. Park, C. Kim, M. Kim and H. Song, Branched copper oxide nanoparticles induce highly selective ethylene production by electrochemical carbon dioxide reduction, *J. Am. Chem. Soc.*, 2019, **141**, 6986–6994.

20 X. Nie, M. R. Esopi, M. J. Janik and A. Asthagiri, Selectivity of CO_2 reduction on copper electrodes: the role of the kinetics of elementary steps, *Angew. Chem., Int. Ed.*, 2013, **52**, 2459–2462.

21 G. Wang, J. Chen, Y. Ding, P. Cai, L. Yi, Y. Li, C. Tu, Y. Hou, Z. Wen and L. Dai, Electrocatalysis for CO_2 conversion: from fundamentals to value-added products, *Chem. Soc. Rev.*, 2021, **50**, 4993–5061.

22 T. Hoang, S. Verma, S. Ma, T. T. Fister, J. Timoshenko and A. I. Frenkel, Nano porous copper-silver alloys by additive-controlled electro-deposition for the selective electroreduction of CO_2 to ethylene and ethanol, *J. Am. Chem. Soc.*, 2018, **140**, 5791–5797.

23 S. Ma, M. Sadakiyo, M. Heima, R. Luo and P. Kenis, Electroreduction of carbon dioxide to hydrocarbons using bimetallic cu-pd catalysts with different mixing patterns, *J. Am. Chem. Soc.*, 2016, **139**, 47–50.

24 X. Yan, C. Chen, Y. Wu, S. Liu, Y. Chen and R. Feng, Efficient electroreduction of CO_2 to C_{2+} products on CeO_2 modified CuO, *Chem. Sci.*, 2021, **12**, 6638–6645.

25 K. Jiang, R. B. Sandberg, A. J. Akey, X. Liu, D. C. Bell, J. K. Nørskov, K. Chan and H. Wang, Metal ion cycling of Cu foil for selective C–C coupling in electrochemical CO_2 reduction, *Nat. Catal.*, 2018, **1**, 111–119.

26 P. De Luna, R. Quintero-Bermudez, C. T. Dinh, M. B. Ross, O. S. Bushuyev, P. Todorovic, T. Regier, S. O. Kelley, P. Yang and E. H. Sargent, Catalyst electro-redeposition controls morphology and oxidation state for selective carbon dioxide reduction, *Nat. Catal.*, 2018, **1**, 103–110.

27 G. De Gregorio, T. Burdyny, A. Loiudice, P. Iyengar, W. A. Smith and R. Buonsanti, Facet-dependent selectivity of Cu catalysts in electrochemical CO_2 reduction at commercially viable current densities, *ACS Catal.*, 2020, **10**, 4854–4862.

28 Y. Gao, Q. Wu, X. Liang, Z. Wang, Z. Zheng, P. Wang, Y. Liu, Y. Dai, M. H. Whangbo and B. Huang, Cu_2O nanoparticles with both {100} and {111} facets for enhancing the selectivity and activity of CO_2 electroreduction to ethylene, *Adv. Sci.*, 2020, **7**, 1902820.

29 Y. Zhou, F. Che, M. Liu, C. Zou, Z. Liang, P. De Luna, H. Yuan, J. Li, Z. Wang, H. Xie, H. Li, P. Chen, E. Bladt, R. Quintero-Bermudez, T. K. Sham, S. Bals, J. Hofkens, D. Sinton, G. Chen and E. H. Sargent, Dopant-induced electron localization drives CO_2 reduction to C_2 hydrocarbons, *Nat. Chem.*, 2018, **10**, 974–980.

30 T. T. Zhuang, Z. Q. Liang, A. Seifitokaldani, Y. Li, P. De Luna, T. Burdyny, F. Che, F. Meng, Y. Min, R. Quintero-Bermudez, C. T. Dinh, Y. Pang, M. Zhong, B. Zhang, J. Li, P.-N. Chen, X. L. Zheng, H. Liang, W. N. Ge, B. J. Ye, D. Sinton, S. H. Yu and E. H. Sargent, Steering post-C-C coupling selectivity enables high efficiency electroreduction of carbon dioxide to multi-carbon alcohols, *Nat. Catal.*, 2018, **1**, 421–428.

31 Y. Wang, Z. Wang, C. T. Dinh, J. Li, A. Ozden, M. G. Kibria, A. Seifitokaldani, C. S. Tan, C. M. Gabardo, M. Luo, H. Zhou, F. Li, Y. Lum, C. McCallum, Y. Xu, M. Liu, A. Proppe, A. Johnston, P. Todorovic, T. T. Zhuang, D. Sinton, S. O. Kelley and E. H. Sargent, Catalyst synthesis under CO_2 electroreduction favours faceting and promotes renewable fuels electrosynthesis, *Nat. Catal.*, 2020, **3**, 98–106.

32 D. Zang, Q. Li, G. Dai, M. Zeng, Y. Huang and Y. Wei, Interface engineering of Mo_8/Cu heterostructures toward highly selective electrochemical reduction of carbon dioxide into acetate, *Appl. Catal., B*, 2021, **281**, 119426.

33 A. Loiudice, P. Lobaccaro, E. A. Kamali, T. Thao, B. H. Huang, J. W. Ager and R. Buonsanti, Tailoring copper nanocrystals towards C_2 products in electrochemical CO_2 reduction, *Angew. Chem., Int. Ed.*, 2016, **55**, 5789–5792.

34 X. Yuan, S. Chen, D. Cheng, L. Li, W. Zhu, D. Zhong, Z. J. Zhao, J. Li, T. Wang and J. Gong, Controllable Cu^0-Cu^+ sites for electrocatalytic reduction of carbon dioxide, *Angew. Chem., Int. Ed.*, 2021, **60**, 15344–15347.

35 J. Albo, G. Beobide, P. Castano and A. Irabien, Methanol Electrosynthesis from CO_2 at Cu_2O/ZnO prompted by pyridine-based aqueous solutions, *J. CO_2 Util.*, 2017, **18**, 164–172.

36 W. Huang, Oxide nanocrystal model catalysts, *Acc. Chem. Res.*, 2016, **49**, 520–527.

37 K. Jiang, R. B. Sandberg, A. J. Akey, X. Liu, D. C. Bell, J. K. Nørskov, K. Chan and H. Wang, Metal ion cycling of Cu foil for selective C–C coupling in electrochemical CO_2 reduction, *Nat. Catal.*, 2018, **1**, 111–119.

38 Z. Z. Wu, F. Y. Gao and M. R. Gao, Regulating the oxidation state of nanomaterials for electrocatalytic CO_2 reduction, *Energy Environ. Sci.*, 2021, **14**, 1121–1139.

39 C. H. Kuo, C. H. Chen and M. H. Huang, Seed-mediated synthesis of monodispersed Cu_2O nanocubes with five different size ranges from 40 to 420 nm, *Adv. Funct. Mater.*, 2007, **17**, 3773–3780.

40 B. Liu, X. Yao, Z. Zhang, C. Li, J. Zhang, P. Wang, J. Zhao, Y. Guo, J. Sun and C. Zhao, Synthesis of Cu_2O nanostructures with tunable crystal facets for electrochemical CO_2 reduction to alcohols, *ACS Appl. Mater. Interfaces*, 2021, **13**, 39165–39177.

41 B. Zhang, J. Zhang, M. Hua, Q. Wan and G. Mo, Highly electrocatalytic ethylene production from CO_2 on nanodefective Cu nanosheets, *J. Am. Chem. Soc.*, 2020, **142**, 13606–13613.

This journal is © the Partner Organisations 2023

Inorg. Chem. Front., 2023, **10**, 240–249 | **247**

42 F. F. Chang, J. C. Wei, Q. Zhang, Z. C. Jia, Y. P. Liu, L. Yang, X. L. Wang and Z. Y. Bai, Modulating the multiple intrinsic properties of platinum–iron alloy nanowires towards enhancing collaborative electrocatalysis, *Mater. Chem. Front.*, 2021, **5**, 8118–8126.

43 F. F. Chang, Y. P. Liu, Q. Zhang, Z. C. Jia, X. L. Wang, L. Yang and Z. Y. Bai, Regulating the lattice strain of platinum–copper catalysts for enhancing collaborative electrocatalysis, *Inorg. Chem. Front.*, 2022, **9**, 249–258.

44 W. Zhang, C. Huang, Q. Xiao, L. Yu, L. Shuai, P. An, J. Zhang, M. Qiu, Z. Ren and Y. Yu, Atypical oxygen-bearing copper boosts ethylene selectivity toward electrocatalytic CO_2 reduction, *J. Am. Chem. Soc.*, 2020, **142**, 11417–11427.

45 J. P. Perdew, K. Burke and M. Ernzerhof, Generalized gradient approximation made simple, *Phys. Rev. Lett.*, 1996, **77**, 3865–3868.

46 A. A. Peterson, F. Abild-Pedersen, F. Studt, J. Rossmeisl and J. K. Norskov, How copper catalyzes the electroreduction of carbon dioxide into hydrocarbon fuels, *Energy Environ. Sci.*, 2010, **3**, 1311–1315.

47 W. Bai, M. Wu, X. Du, W. Gong, Y. Ding, C. Song and L. Liu, Synergistic effect of multiple-phase $rGO/CuO/Cu_2O$ heterostructures for boosting photocatalytic activity and durability, *Appl. Surf. Sci.*, 2021, **544**, 148607.

48 P. D. Luna, R. Quintero-Bermudez, C. T. Dinh, M. B. Ross, O. S. Bushuyev, P. Todorovi, T. Regier, S. O. Kelley, P. Yang and E. H. Sargent, Catalyst electro-redeposition controls morphology and oxidation state for selective carbon dioxide reduction, *Nat. Catal.*, 2018, **1**, 103–110.

49 T. Ghodselahi, M. A. Vesaghi, A. Shafiekhani, A. Baghizadeh and M. Lameii, XPS study of the $Cu@Cu_2O$ core-shell nanoparticles, *Appl. Surf. Sci.*, 2008, **255**, 2730–2734.

50 D. X. Tan, J. L. Zhang, X. Y. Cheng, X. N. Tan, J. B. Shi, B. X. Zhang, B. X. Han, L. R. Zheng and J. Zhang, Cu_xNi_y alloy nanoparticles embedded in a nitrogen-carbon network for efficient conversion of carbon dioxide, *Chem. Sci.*, 2019, **10**, 4491–4496.

51 C. M. Gabardo, A. Ozden, C. T. Dinh, J. Li, Y. Wang, J. P. Edwards, Y. Xu, C. McCallum, L. Tao, Z. Q. Liang, M. Luo, X. Wang, H. Li, C. P. O'Brien, C. S. Tan, D. H. R. Nam, R. Quintero-Bermudez, T.-T. Zhuang, Y. C. Li, Z. Han, R. D. Britt, D. Sinton, T. Agapie, J. C. Peters and E. H. Sargent, Molecular tuning of CO_2-to-ethylene conversion, *Nature*, 2020, **577**, 509–513.

52 C. T. Dinh, T. Burdyny, M. G. Kibria, A. Seifitokaldani, C. M. Gabardo, F. P. García de Arquer, A. Kiani, J. P. Edwards, P. De Luna, O. S. Bushuyev, C. Zou, R. Quintero-Bermudez, Y. Pang, D. Sinton and E. H. Sargent, CO_2 electroreduction to ethylene via hydroxide-mediated copper catalysis at an abrupt interface, *Science*, 2018, **360**, 783–787.

53 Z. Liang, T. Zhuang, A. Seifitokaldani, J. Li, C. Huang, C. Tan, Y. Li, P. De Luna, C. T. Dinh, Y. Hu, Q. Xiao, P. Hsieh, Y. Wang, F. Li, R. Quintero-Bermudez, Y. Zhou, P. Chen, Y. Pang, S. Lo, L. J. Chen, H. Tan, Z. Xu, S. Zhao, D. Sinton and E. Sargent, Copper-on-nitride enhances the stable electrosynthesis of multi-carbon products from CO_2, *Nat. Commun.*, 2018, **9**, 3828.

54 A. Loiudice, P. Lobaccaro, E. A. Kamali, T. Thao, B. H. Huang, J. W. Ager and R. Buonsanti, Tailoring copper nanocrystals towards C_2 products in electrochemical CO_2 reduction, *Angew. Chem., Int. Ed.*, 2016, **55**, 5789–5792.

55 H. Jung, S. Y. Lee, C. W. Lee, M. K. Cho, D. H. Won, C. Kim, H. S. Oh, B. K. Min and Y. J. Hwang, Electrochemical fragmentation of Cu_2O nanoparticles enhancing selective C-C coupling from CO_2 reduction reaction, *J. Am. Chem. Soc.*, 2019, **141**, 4624–4633.

56 Y. Zhou, F. Che, M. Liu, C. Zou, Z. Liang, P. De Luna, H. Yuan, J. Li, Z. Wang, H. Xie, H. Li, P. Chen, E. Bladt, R. Quintero-Bermudez, T. Sham, S. Bals, J. Hofkens, D. Sinton, G. Chen and E. Sargent, Dopant-induced electron localization drives CO_2 reduction to C_2 hydrocarbons, *Nat. Chem.*, 2018, **10**, 974–980.

57 W. Ma, S. Xie, T. Liu, Q. Fan, J. Ye, F. Sun, Z. Jiang, Q. Zhang, J. Cheng and Y. Wang, Electrocatalytic reduction of CO_2 to ethylene and ethanol through hydrogen-assisted C–C coupling over fluorine-modified copper, *Nat. Catal.*, 2020, **3**, 478–487.

58 C. S. Chen, J. H. Wan and B. S. Yeo, Electrochemical reduction of carbon dioxide to ethane using nanostructured Cu_2O-derived copper catalyst and palladium(II) chloride, *J. Phys. Chem. C*, 2015, **119**, 26875–26882.

59 M. Zhong, K. Tran, Y. Min, C. Wang, Z. Wang, C. T. Dinh, P. De Luna, Z. Yu, A. S. Rasouli, P. Brodersen, S. Sun, O. Voznyy, C. S. Tan, M. Askerka, F. Che, M. Liu, A. Seifitokaldani, Y. Pang, S. C. Lo, A. Ip, Z. Ulissi and E. H. Sargent, Accelerated discovery of CO_2 electrocatalysts using active machine learning, *Nature*, 2020, **581**, 178.

60 D. Wu, C. Dong, D. Wu, J. Fu, H. Liu, S. Hu, Z. Jiang, S. Qiao and X. Du, Cuprous ions embedded in ceria lattice for selective and stable electrochemical reduction of carbon dioxide to ethylene, *J. Mater. Chem. A*, 2018, **6**, 9373–9377.

61 D. Tan, J. Zhang, L. Yao, X. Tan, X. Cheng, Q. Wan, B. Han, L. Zheng and J. Zhang, Multi-shelled CuO microboxes for carbon dioxide reduction to ethylene, *Nano Res.*, 2020, **13**, 768–774.

62 C. Choi, S. Kwon, T. Cheng, M. Xu, P. Tieu, C. Lee, J. Cai, H. M. Lee, X. Pan, X. Duan, W. A. Goddard and Y. Huang, Highly active and stable stepped Cu surface for enhanced electrochemical CO_2 reduction to C_2H_4, *Nat. Catal.*, 2020, **3**, 804–812.

63 J. Gong, D. Zhong, Z.-J. Zhao, Q. Zhao, D. Cheng and B. Liu, Coupling of Cu(100) and (110) facets promotes carbon dioxide conversion to hydrocarbons and alcohols, *Angew. Chem., Int. Ed.*, 2021, **60**, 4929–4935.

64 H. A. Hansen, J. B. Varley, A. A. Peterson and J. K. Nørskov, Understanding trends in the electrocatalytic activity of metals and enzymes for CO_2 reduction to CO, *J. Phys. Chem. Lett.*, 2013, **4**, 388–392.

65 J. T. Feaster, C. Shi, E. R. Cave, T. Hatsukade, D. N. Abram, K. P. Kuhl, C. Hahn, J. K. Nørskov and T. F. Jaramillo, Understanding selectivity for the electrochemical reduction of carbon dioxide to formic acid and carbon monoxide on metal electrodes, *ACS Catal.*, 2017, **7**, 4822–4827.

66 J. Gao, H. Zhang, X. Guo, J. Luo, S. M. Zakeeruddin, D. Ren and M. Grätzel, Selective C−C coupling in carbon dioxide electroreduction via efficient spillover of intermediates as supported by operando raman spectroscopy, *J. Am. Chem. Soc.*, 2019, **141**, 18704–18714.

67 J. Applied Energy Gao, H. Zhang, X. Guo, J. Luo, S. M. Zakeeruddin, D. Ren and M. Grätzel, Selective C−C coupling in carbon dioxide electroreduction via efficient spillover of intermediates as supported by operando Raman spectroscopy, *J. Am. Chem. Soc.*, 2019, **141**, 18704–18714.

68 M. B. Ross, C. T. Dinh, Y. Li, D. Kim, P. De Luna, E. H. Sargent and P. Yang, Tunable Cu enrichment enables designer syngas electrosynthesis from CO_2, *J. Am. Chem. Soc.*, 2017, **139**, 9359–9363.

69 Y. Kim, S. Park, S. J. Shin, W. Choi, B. K. Min, H. Kim, W. Kim and Y. J. Hwang, Time-resolved observation of C−C coupling intermediates on Cu electrodes for selective electrochemical CO_2 reduction, *Energy Environ. Sci.*, 2020, **13**, 4301–4311.

70 Z. Z. Niu, F. Y. Gao, X. L. Zhang, P. P. Yang, R. Liu, L. P. Chi, Z. Z. Wu, S. Qin, X. Yu and M. R. Gao, Hierarchical copper with inherent hydrophobicity mitigates electrode flooding for high-rate CO_2 electroreduction to multicarbon products, *J. Am. Chem. Soc.*, 2021, **143**, 8011–8021.

71 Y. Jiang, X. Wang, D. Duan, C. He, J. Ma, W. Zhang, H. Liu, R. Long, Z. Li, T. Kong, X. J. Loh, L. Song, E. Ye and Y. Xiong, Structural reconstruction of Cu_2O superparticles toward electrocatalytic CO_2 reduction with high C_{2+} products selectivity, *Adv. Sci.*, 2022, **9**, 2105292.

This journal is © the Partner Organisations 2023

Inorg. Chem. Front., 2023, **10**, 240–249 | **249**